Sensing and Bio-Sensing Research 26 (2019) 100300

Contents lists available at ScienceDirect

Sensing and Bio-Sensing Research

journal homepage: www.elsevier.com/locate/sbsr

Error compensation in force sensing resistors

Elkin I. Gutiérrez Velásquez[a,*], Víctor Gómez[b], Leonel Paredes-Madrid[a], Henry A. Colorado[c]

[a] Faculty of Mechanic, Electronic and Biomedical Engineering, Universidad Antonio Nariño, Medellín, 050022, Colombia
[b] Fundación Universitaria Agraria de Colombia, Uniagraria, Calle 170 # 54a – 10, Bogotá, Colombia
[c] CCComposites Laboratory, Universidad de Antioquia UdeA, Calle 70 No. 52-21, Medellín, Colombia

ARTICLE INFO

Keywords:
Force sensor
Pressure sensor
FSR
Piezoresistive sensor

ABSTRACT

The force-sensing resistors (FSRs), like the other types of sensors, present a series of errors that make their use limited to applications that do not require high levels of precision. Among the most outstanding errors of this type of sensors are the hysteresis, non-linearity and drift errors. A methodology that seeks to reduce these errors by analyzing alternative correlations to those proposed by manufacturers based on simple linear correlations is performed. This paper presents the results of a research aimed at the characterization of a Tekscan A201-1 sensor, in which several correlations that combine the voltage and capacitance readings, were used to obtain an improved response signal that reduces hysteresis errors, non-linear and derives in FSRs. In this study, eight sensors to which a predefined force pattern was applied were analyzed. The obtained results allowed to reach a significant reduction of the error in comparison with the linear regression method proposed by the manufacturer of these force sensors. Finally, the correlations evaluated and the reductions of errors obtained by the methodology used are presented.

1. Introduction

Force Sensing Resistors (FSRs) are two terminal devices manufactured from polymer blends and conductive nanoparticles. FSRs have found great acceptance in research due to its remarkable piezoresistive response. When a FSR is mechanically loaded, variation of resistance occurs which can be correlated in an inverse-proportionally fashion with the input force/stress; this behavior is known in literature as negative piezoresistive behavior [28]. However, some FSRs exhibit positive piezoresistive coefficient, i.e. incremental stresses produce larger resistances [29]. Conditioning circuits are typically employed to convert resistance variations to voltage variations; for this purpose, voltage dividers [33] and/or inverting amplifiers [30] are deployed in the final application. Numerous industrial applications derive from precise force measurements to provide reliable records and outstanding developments [1].

There are several models of force sensors available in the market, which can be grouped mainly by their range of measurement or presentation. Among these, the load cells stand out for their flexibility, high linearity, and good precision, however, these robust components become an unfeasible option for several applications in which lightweight and compact components are required. This is the case in biomechanical studies, where non-invasive and precise force measurements are necessary. This type of application requires that the transducers used be installed with the least possible interference in the human or animal studied to avoid discomfort during movement. Therefore, the sensors used in biomechanical investigations should be small and of low thickness or the variables to be measured should be tracked remotely when possible [2].

The realization of precise readings of position and inertia has been solved with encoders and Inertial Measurement Units (IMU). However, if such sensors become excessively bulky, high-speed cameras can be used as an alternative [3,4]. On the other hand, performing accurate force readings has always been a difficult task in biomechanical analysis because force can not be monitored remotely.

The force sensor resistors (FSR) are low-cost force sensors that can be easily incorporated into numerous biomechanical applications [5,6]. However, the main reasons for its extensive use are its lower thickness and reduced weight, which are highly desirable features when trying to execute non-invasive force measurements [7]. Another reason for its wide acceptance is the simple interface circuit needed to read the sensor output, for example, voltage dividers or inverting amplifiers. When an inverting amplifier is used as the driving circuit, see Fig. 1a, it is possible to estimate sensor's conductance ($1/R$) by measuring the amplifier output voltage (V_{o1}). On the other hand, when a voltage divider is used, see Fig. 1b, the sensor resistance (R_s) is measured by means of V_{o2}.

* Corresponding author.
E-mail address: elkin.gutierrez@uan.edu.co (E.I.G. Velásquez).

https://doi.org/10.1016/j.sbsr.2019.100300
Received 4 April 2019; Received in revised form 22 September 2019; Accepted 24 September 2019

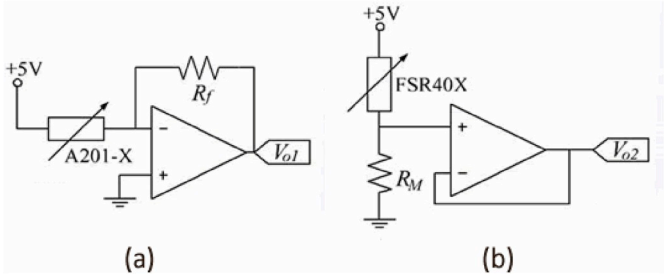

Fig. 1. Driving circuits for: (a) FlexiForce A201-X, (b) Interlink FSR40X. Adapted from Ref. [19].

Commercially available FSRs can be found in different nominal forms and ranges. Interlink Electronics [8], produce disk-shaped FSRs (FSR400 and FSR402) and square FSRs (FSR406 and FSR408). Tekscan Inc., of South Boston, MA, offers disk-shaped (A201-1, A201-25 and A201-100) and several customizable FSRs in its product catalogue [9]. Unfortunately, the overall performance of FSRs is poor compared to well-known force detection solutions, such as load cells and strain gauges. The preceding works of *Lebosse* et al. and *Komi* et al. [10,11] present a complete review of the restrictions of the FSRs. Hysteresis and drift are normally one or two orders of magnitude greater in the FSRs than in the load cells. These circumstances are the main disadvantage for the wide use of FSRs in industrial and research uses, but a profuse effort is currently being made to increase their performance. In this regard, Saadeh and Trabia demonstrated that the hysteresis error could be minimized through the application of modeling and compensation techniques such as Hammerstein–Wiener model [3]. Likewise, previous authors' work demonstrated that the Preisach operator could be used as an effective strategy to minimize the hysteresis error in FSRs [DYNA].

FSRs have been used in abundant biomechanical applications of prosthetic control and pressure measurements [12–14] through gait [15,16] and telerobotic investigations [17,18], among many other biomechanical applications.

Nevertheless, FSRs have restrictions: the sensor drift and hysteresis have an adverse effect over their repeatability and accuracy [19–21]. In addition, changes in accuracy and increases in drift error have been shown in prosthetic purposes [22], even though can be minimized by the use of enhanced algorithms to compute the applied forces [20,23].

A current trend in the FSR research is to model the response of the sensors, in order to compensate their hysteresis and drift, with many relevant works exposed in this field [6,10,19,24]. In the same way, a preceding work has revealed that the A201 sensors, which work on the piezoresistive principle, are also capable of showing a piezocapacitive response, allowing a reduction in the mean square error (MSE) of force [25]. The reduction in MSE can be obtained by increasing the complexity of the driving circuit, which can be excessively difficult for some applications with power or space limitations.

The technique presented here involves of using a correlation that makes combined use of the voltage and capacitance signals, and making use of the simple circuit as shown in Fig. 1a and b, when using FlexiForce or Interlink sensors respectively. The proposed methodology does not require a considerable computational effort for its execution, and allows a significant reduction in the MSE error of the measured force. To obtain a valid generalization of the results, eight FlexiForce A201-1 sensors were used. The used sensor matches the range of force typically required (4.5 N) in biomechanical applications concerning gripping operations. However, the method analyzed below is applicable to other FSR models.

2. Experimental configuration

Previous work by *Paredes-Madrid* et al. shows that A201-X sensors can be modeled electrically as a parallel device $R_s - C_s$ as shown in

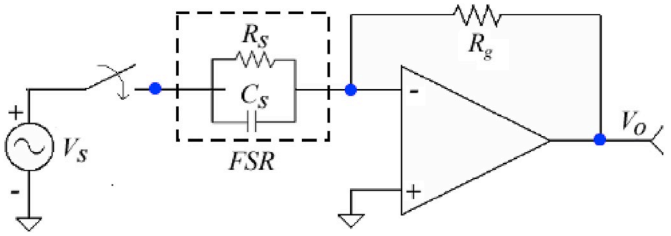

Fig. 2. Amplifier in inverting configuration and equivalent circuit for an A201-X sensor (enclosed within dashed lines).

Fig. 2 [25]. In which, R_s shows a hyperbolic dependence with the applied force (F). For linearization purposes, conductance variations, measured through V_o, have been preferably used in several studies to estimate the applied force F [10,19,25]; by the expression:

$$F = mV_o + b \tag{1}$$

Where m and b are obtained from the least squares fitting method. The sensor characterization procedure may be associated only with increasing forces or a combination of increasing-decreasing forces, as is the case of the present study. It should be noted that the application of any pattern of forces produces a significant effect on the values m and b, given the hysteresis in the device. The test bench for the characterization and testing of sensors comprises electrical and mechanical sensors/actuators as described below.

For the circuit in Fig. 3, the variation in resistance R_s and capacitance C_s can be studied as a function of the changes in force by the following differential equation:

$$\frac{V_s}{R_s} + C_s\frac{dV_s}{dt} = -\frac{V_o}{R_g}$$

with a sinusoidal voltage input ($A_s \sin(2\pi ft)$), the following expression is obtained for V_o:

$$V_o = -A_s R_s\left(\frac{\sin(2\pi ft)}{R_s} + 2\pi f C_s \cos(2\pi ft)\right) \tag{3}$$

Equation (3) can be rewritten as a sinusoidal function with a phase change (φ) such as:

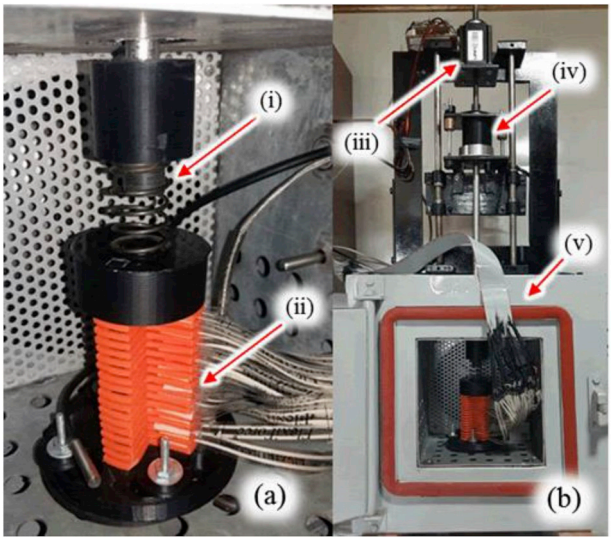

Fig. 3. Test bench for the characterization of A201-X sensors. (a) Close-up image showing spring (i) for mechanical compliance of the test bench and a sensor set A201-1 (ii) arranged in a sandwich configuration. (b) Image of the test bench showing the stepper motor (iii), the load cell LCHD-5 (iv) and the temperature chamber (v).

$$V_o = A_o \sin(2\pi ft + \varphi) \quad (4)$$

Then, by joining Eqs. (3) and (4) results in:

$$R_s = \frac{R_g A_s}{A_o \cos(\varphi)} \quad (5)$$

and

$$C_s = \frac{A_o \sin(\varphi)}{R_g A_s 2\pi f} \quad (6)$$

where the output amplitude (A_o) and the phase shift (φ) were measured experimentally for every exerted force.

2.1. Mechanical configuration

To obtain a compensation between the nominal force and the resolution, a linear stepper motor with a spring has been arranged to apply precise forces in the sensors under test, as shown in Fig. 3. The mechanical conformity of the test bench can be modified through the stiffness constant of the spring. Therefore, the spring can be exchanged to modify the applied force according to the needs of the experiment. The test bench allows to register data of up to sixteen sensors simultaneously. The sensitivity of the system was determined by the resolution of the load cell, which is 1.4 mN and a maximum load rate of 22.6 N/s. These features were adequate to emulate the profiles of force exerted during the grip operations, such as those reported previously [26].

The sensors were placed in a sandwich configuration and then installed inside a temperature-controlled chamber. The operating temperature was set at 25 °C ± 1 °C to avoid undesired effects caused by thermal drift, see Fig. 3b. Bearing in mind that the main objective of this article is to reduce the error in the determination of force, changes in temperature were not considered as an additional variable. In addition, as can be seen in the configuration shown in Fig. 3. The stacking structure of Fig. 3a ensured that the force applied to a sensor is transferred to the one immediately below; this was possible by the design of the sensor's holder with pucks on the opposite side, see Fig. 3c. Likewise, separation between sensors was possible from the pucks which have the shape of round bulge as depicted in Fig. 3c. The puck diameter is equal to 7.7 mm, which accounts for 66% of the sensor sensitive area, i.e. the sensitive area of the FlexiForce sensor is equal to 71 mm^2, whereas puck's area is 47 mm^2. Stacking was possible by arranging multiple pucks on top of each other as shown in Fig. 3a. A square key was installed through each puck's hollow; this ensured proper alignment of the sensors as shown in the final arrangement of Fig. 3a and b. Each puck has two hollows (see Fig. 3c), and consequently, two square keys were used in the final arrangement. Each puck has a weight of 2 gr. The weight of the pucks was accounted in the error calculation of Section 4. This is important because the sensors at the bottom are more heavily loaded than the ones on top.

2.2. Electrical installation

Regardless of the type of sourcing (DC or AC), the circuit from Fig. 1a was used as the driving circuit for the sensors. However, in order to, simultaneously, handle multiple FSRs, a time-multiplexed scheme was implemented; it comprised analog multiplexers (ADG444) for reading *Vo* as shown in Fig. 4. This setup was used for gathering the data reported in Fig. 5 through Fig. 13. At this point, it must clarified that the sketch from Fig. 2 is basically the same as that from Fig. 1, with the only difference that in Fig. 2, the FSR was modeled as an RC device when sourced by an AC signal. The feedback resistance (R_f) was set to 10 kΩ, and the supply voltage (V_S) was set to -1 V for both DC and AC sourcing (As = -1 V as defined in Eq.(3), (5) and (6)). The frequency of the AC sourcing, f, was set to 4 KHz. The output voltage Vo was digitalized from a 16 bit ADC available in the board NI 9205.

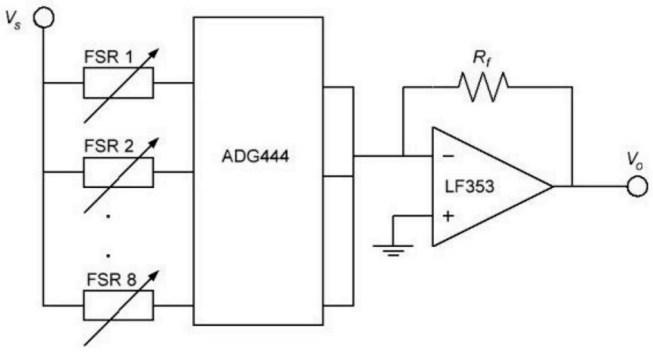

Fig. 4. Multiplexed circuit for reading sensor output voltage (V_o) from eight FlexiForce A201-1 sensors. Adapted from Ref. [20].

It should be noted that FlexiForce sensors exhibit a subtle saturation effect in the form of a hyperbolic tangent with respect to V_s variations. This effect prevents m and b from being recalculated when changing V_s since k in equation (2) changes from one sensor to another [25]. In practice, this implies that equation (1) is valid only for constant V_s during sensor operation:

$$V_o = -(mF + b)\text{atanh}(V_s/k) \quad (2)$$

3. Preliminary considerations

In this analysis, FlexiForce A201-1 sensors that have a nominal capacity of 1 lbF (4.4 N), were used. These sensors are manufactured by Tekscan, Inc (Boston, MA). The manufacturing process involves the preparation of a blend of insulting polymer (typically elastomer) and carbon black, this latter plays the role of the conductive phase in the mix [31,32]. The sensing area is round with a diameter of 9.53 mm And 0.2 mm thick [9]. In total, the voltage and capacitance responses of a set of eight Tekscan A201-1 force sensors, which were exposed to a predetermined force pattern, were evaluated and correlated. Figs. 5 and 6 show, respectively, the voltage and capacitance responses compared to the applied force pattern, for sensor 1 (S1).

From these figures, it is observed that although there is a proportionality between the voltage and capacitance registers with the applied force, the response of the readings does not coincide exactly with the applied force patterns. Likewise, both voltage and capacitance responses exhibit some inertia, according to which the detected signals tend to continue to increase when the applied force remains constant. It is also observed that this tendency is greater in the voltage responses than in the capacitance ones.

Fig. 6 shows the voltage and capacitance responses plotted against the applied force for the force pattern used on the sensor 1 with its respective linear trend lines. In this figure, it can be seen that for the applied force pattern, both voltage and capacitance readings exhibit a certain degree of fluctuation due to the hysteresis of the sensor. In addition, such responses are not inherently linear, especially in the case of capacitance responses. Moreover, Fig. 6 shows how the fluctuation is comparatively smaller for capacitance responses and occurs to a lesser degree for smaller load values.

4. Error analysis

In this study, the estimation of the error will be based on three metrics: the first consists of the determination of the nonliniearity error (NL) which is defined as the maximum difference between the load applied and the load registered, divided by the actual load value (P) in a specified range of load (see Fig. 7a). Therefore, the Nonlinearity error NL_e was calculated as:

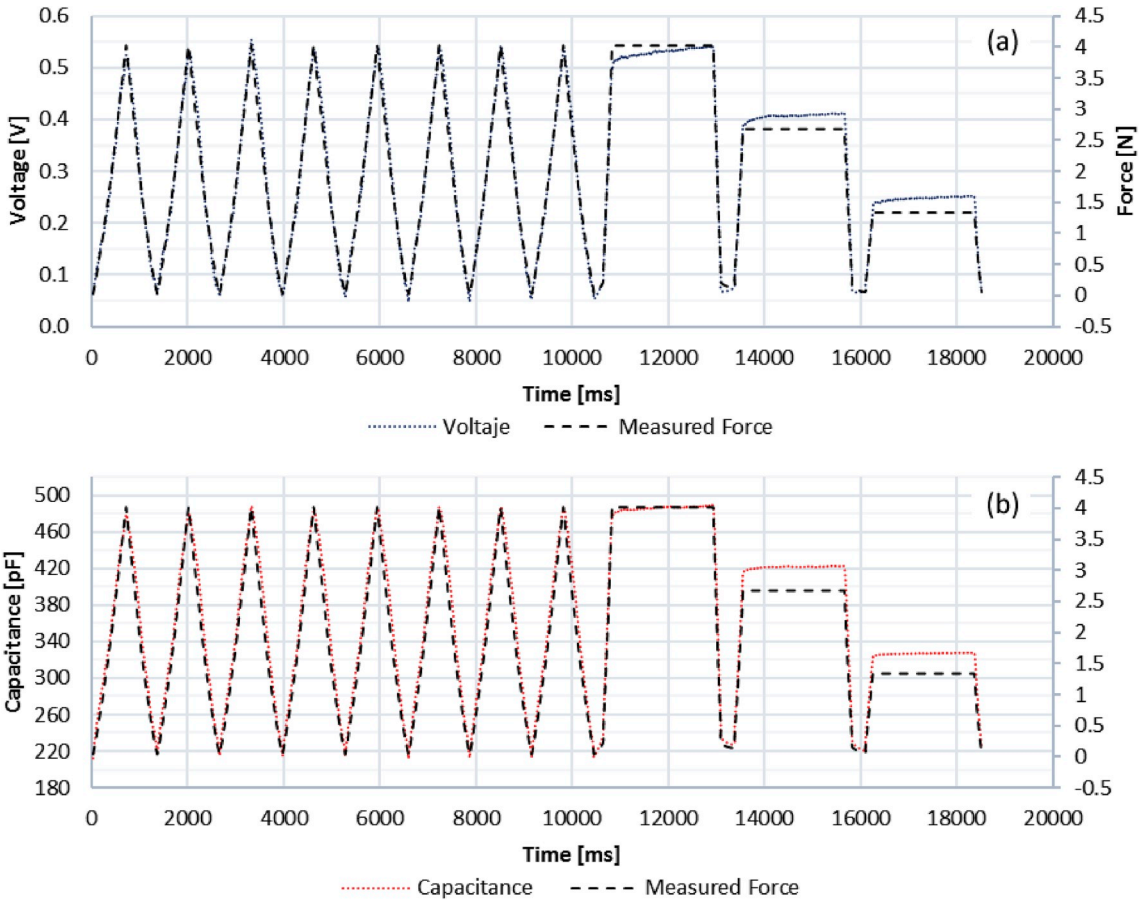

Fig. 5. Response of the S1 sensor, compared to the applied force pattern. (a) Voltage, (b) Capacitance.

$$NL_e = \frac{error_{max}}{P} \tag{3}$$

The second metric consists of the estimation of the hysteresis error, which is defined as the maximum difference between the ascending and descending load registers within a specified range of the sensor, when applying a charge-discharge cycle, divided by the actual load value (P) in the specified cycle (see Fig. 7b). Therefore, the hysteresis error H_e was calculated as:

$$H_e = \frac{error_{max}}{P} \tag{4}$$

The third metric is the determination of stability, which is the ability of a sensing device to give the same output when used to measure a constant input over an interval of time. The term "drift" is used to indicate the change in the output that occurs over a interval of time (See Fig. 7c). The drift error D_e was calculated as:

$$D_e = \frac{error_{max} - error_{min}}{\Delta t} \tag{5}$$

5. Experimental results and analysis

The load pattern used in this analysis was applied with the device previously described and shown in Fig. 3, in which incremental loads were applied up to a maximum load of 4 N, during a period of 18.5 s, with increments of 10 ms.

From the voltage and capacitance responses, the applied force was correlated, both linearly and by other models based on the voltage and capacitance responses for each of the sensors. For this, correlations able to predict the force applied based on the combined voltage, capacitance and voltage and capacitance records have been developed. The correlations evaluated, as well as the designation used in this study for each of them, are presented in Table 1.

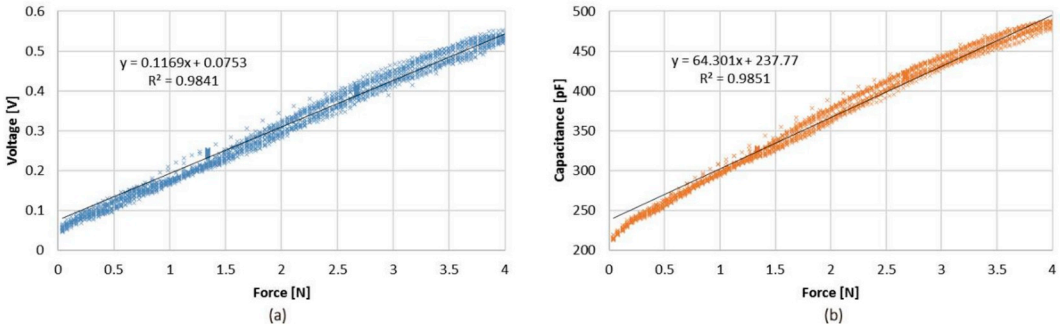

Fig. 6. Sensor 1 readings versus load. (a) Voltage, (b) Capacitance.

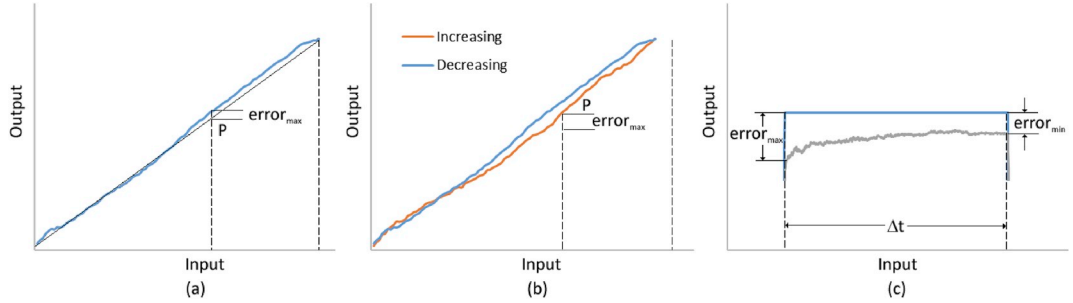

Fig. 7. Estimation of the hysteresis error. (a) Nonlinearity error, (b) hysteresis error, (c) drift error.

Table 1
Set of assessed correlations.

Correlation	Parameters	Designation
Linear	Voltage	P1(V)
Linear	Capacitance	P1(C)
Linear	Voltage, Capacitance	P1(V, C)
Power function	Voltage	PF(V)
Power function	Capacitance	PF(C)
Power function	Voltage, Capacitance	PF(V, C)
Exponential function	Voltage, Capacitance	Exp (V, C)

To determine the coefficients of the different proposed correlations, 500 randomly chosen records were taken from 3514 records for sensor 1. Then, with the help of the commercial software ModeFrontier [27], the coefficients and the regression parameter (R^2) that showed a better fit to the applied force pattern were obtained. The respective coefficients and regression parameters are summarized in Table 2, as well as the expressions used for the analysis.

According to the data shown in Table 2, the correlation that best fitted the real force records was the corresponding to the power function, considering the voltage and capacitance registers as input parameters. This evaluation was confirmed in Fig. 8, which shows the force records predicted by the correlations listed in Table 2 for sensor 1. This figure shows the best adjustment of the correlation of the power function, where a remarkable reduction of the deviation of the output signal is observed in comparison with the independent voltage and capacitance registers presented in Fig. 5. Similar analysis was carried out for the other sensors. Accordingly, the coefficients for the power function correlation of the eight sensors analyzed were established and summarized in Table 3.

5.1. Calculation of errors

In order to quantify the influence of the load pattern applied on the error of the sensors, the data obtained, according to the load pattern shown in Fig. 5, were divided into two sets. The first set was made up of the ramp-type data of the first data interval, which corresponds to eight load-unload cycles. The force records obtained by the eight sensors for this first data set, as well as the absolute error obtained in relation to the applied force pattern are shown in Fig. 9a, for the data obtained by means of the linear correlation, based in voltage only, suggested by the sensor manufacturers, which will henceforth be called correlation P1. Similarly, in Fig. 9b, the force and absolute error registers are shown when using the power function correlation, based on voltage and capacitance readings, proposed in this analysis, which will henceforth be referred to as the PF correlation.

The second data set corresponds to the data in which constant load was applied during a defined time interval, which corresponds to the three final cycles, in which the load was kept constant for a period of 2 s. The force records obtained by the eight sensors for this second data set, as well as the absolute error obtained in relation to the applied force pattern are shown in Fig. 10a for the data obtained by means of the correlation P1. Similarly, the force and absolute error records are shown in Fig. 10b when using the PF correlation.

5.1.1. Hysteresis error

For the determination of hysteresis errors, the eight load-discharge cycles of the first group of data were analyzed in the eight sensors evaluated. The hysteresis error H_e was calculated according to Eq. (3). For this, the errors obtained by using both a linear model (P1) and a power function model (PF) were analyzed. The response signal obtained by the model P1 is shown in Fig. 10a, and the response signal obtained with the model PF is shown in Fig. 10b. Likewise, in Fig. 11 the hysteresis errors obtained in each one of the evaluated sensors were compared when using the linear regression model (P1) with the power function regression model (PF). Hysteresis errors were obtained as the average hysteresis error calculated in each of the eight load-discharge cycles analyzed. In Fig. 11, it can be seen how, by using the PF regression model instead of the P1 regression model, significant reductions in hysteresis error of up to 39% are obtained, as is the case with the S5 sensor. It should be noted that in the case of sensors S2, S4 and S6 a very slight increase in hysteresis error of less than 3% is obtained.

5.1.2. Nonlinearity error

The evaluation of the non-linearity errors NL_e was determined in each of the loading and unloading sections of the first data set for each of the evaluated sensors, in accordance with Eq. (4). Nonlinearity errors in the 16 straight segments were averaged for each sensor and are presented in Fig. 12 using both the P1 regression model and the PF

Table 2
Coefficients and regression parameter for sensor 1.

Label	Correlation	a_0	a_1	a_2	b_1	b_2	R^2
P1(V)	$a_0 + a_1 \cdot V$	−0.548	8.312	–	–	–	0.970
P1(C)	$a_0 + a_1 \cdot C$	−3.458	0.015	–	–	–	0.966
P1(V,C)	$a_0 + a_1 \cdot C + a_2 \cdot V$	−1.475	4.7E-3	5.682	–	–	0.970
PF(V)	$a_0 + a_1 \cdot V^{b_1}$	−0.075	9.129	–	1.291	–	0.980
PF(C)	$a_0 + a_1 \cdot C^{b_1}$	−0.776	1.4E-5	–	2.059	–	0.990
PF(V,C)	$a_0 + a_1 \cdot C^{b_1} + a_2 \cdot V^{b_2}$	0.262	3.2E-7	−0.132	2.639	−0.561	0.992
Exp (V,C)	$a_0 + a_1 \cdot e^{C \cdot b_1} + a_2 \cdot e^{V \cdot b_2}$	−5.191	−1.798	4.991	−5.846	1.146	0.980

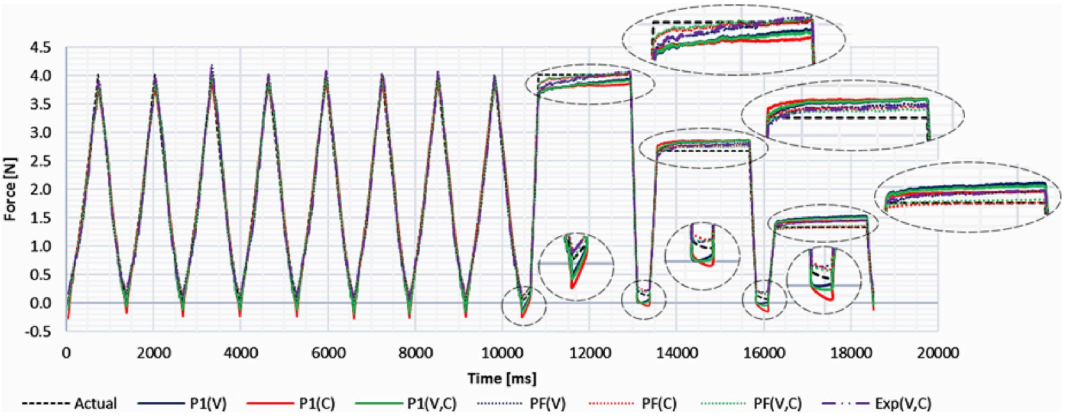

Fig. 8. Comparison of the force records corrected according to the correlations shown in Table 2 for sensor 1.

Table 3
Coefficients for power function correlations for all sensor analyzed.

Sensor	a_0	a_1	a_2	b_1	b_2
S1	0.262	3.2E-7	−0.132	2.639	−0.561
S2	−0.919	3.7E-6	4.2E-7	1.920	0.743
S3	−1.606	5.1E-5	−0.038	8.638	0.987
S4	−0.675	6E-24	7.237	2.887	3.645
S5	−1.031	1.1E-7	−9.393	2.887	3.645
S6	−0.494	6.105	9.580	−9.900	1.260
S7	−2.848	1E-16	6.713	5.964	0.383
S8	0.734	3.2E-9	−0.195	3.372	−0.792

regression model. In Fig. 12, it can be seen how the PF regression model shows a better behavior in relation to the P1 model, since it shows significant reductions in all the evaluated sensors.

5.1.3. Drift error

The drift error was determined taking into consideration the second data set shown in Fig. 10. For this, the drift errors were calculated and averaged in the three horizontal segments according to the expression for D_e shown in Eq. (5), for the sensors evaluated. The results obtained by this analysis are shown in Fig. 13. From these results, it can be seen that the PF regression model shows a better behavior in relation to the P1 model. Reductions in the drift error were revealed in all the sensors

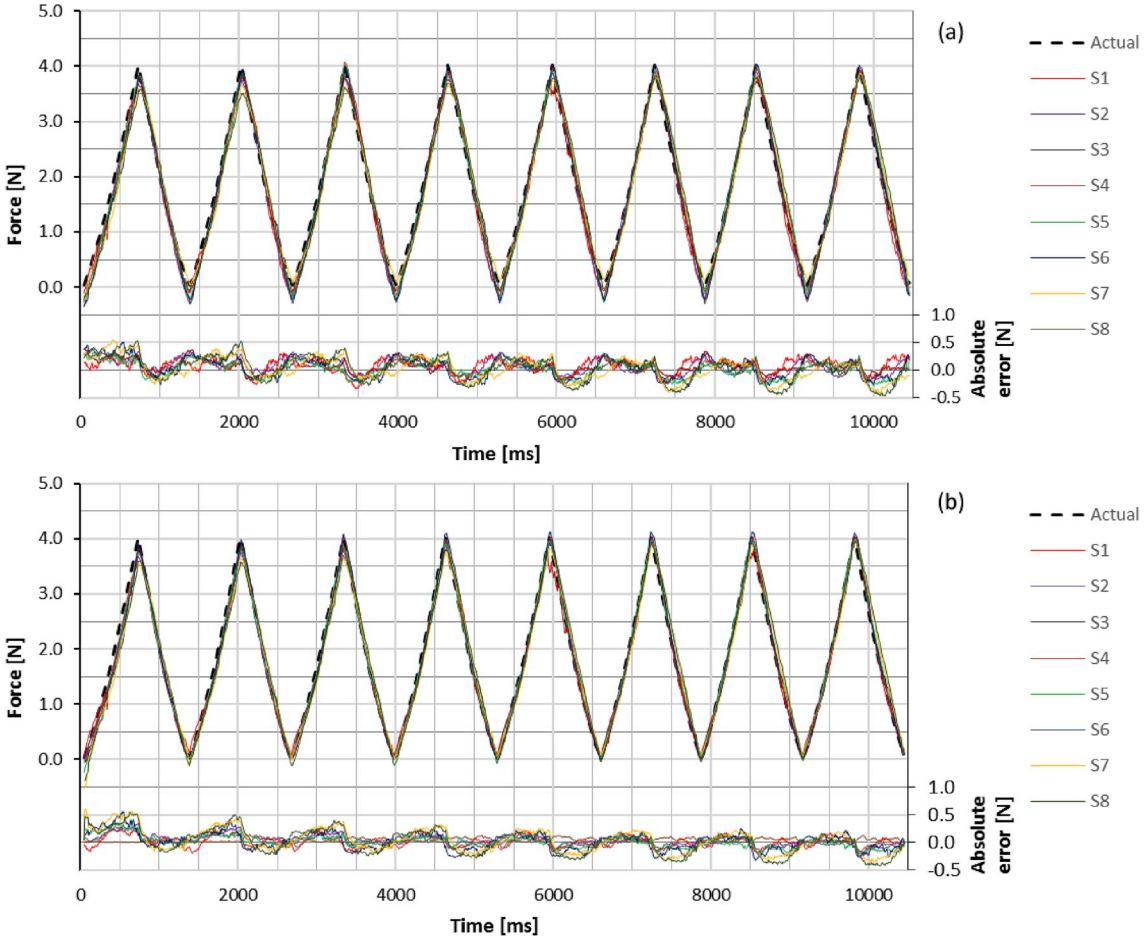

Fig. 9. Force records and absolute error obtained by the sensors tested for the first set of data. (a) Using linear correlation, (b) using power function correlation.

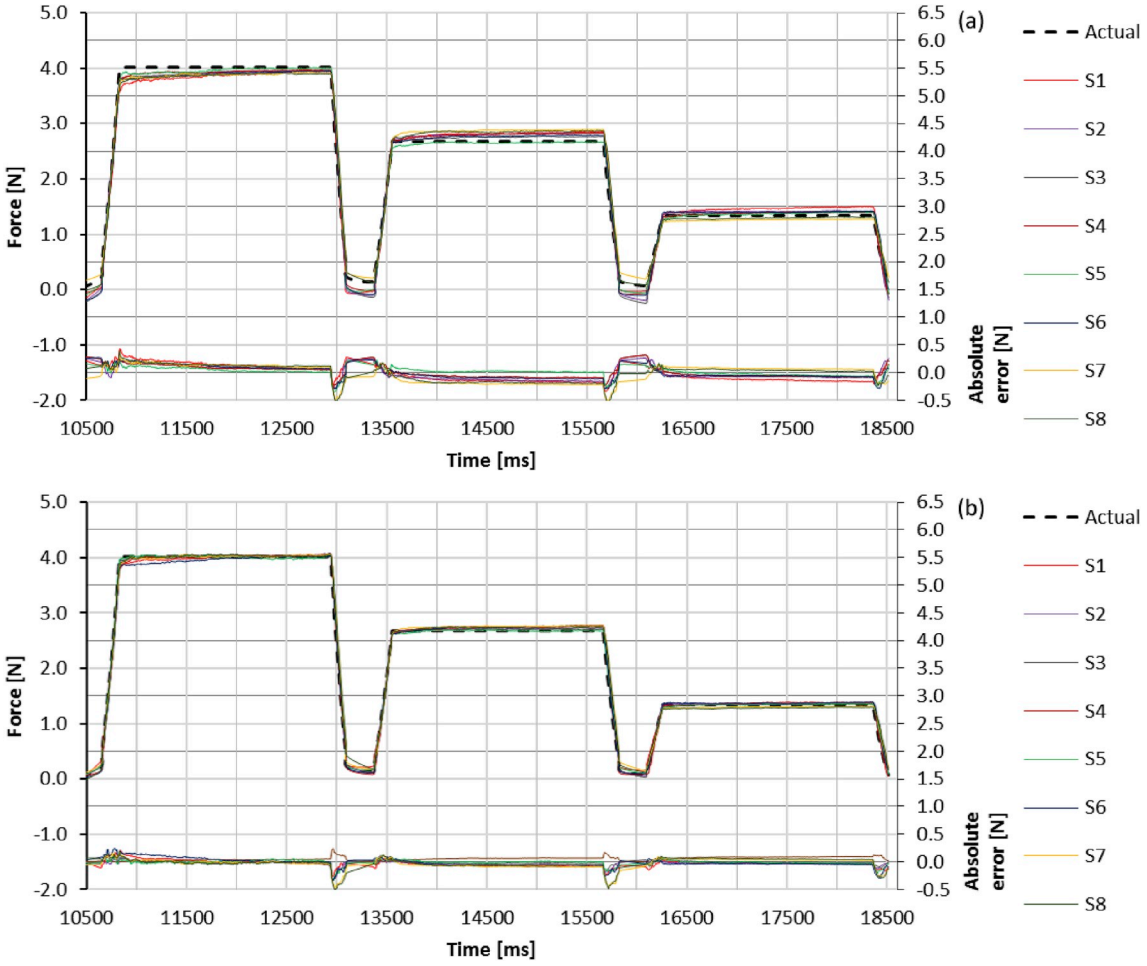

Fig. 10. Comparison of the force records corrected according to the correlations shown in Table 2 for sensor 1. (a) Using linear correlation, (b) using power function correlation.

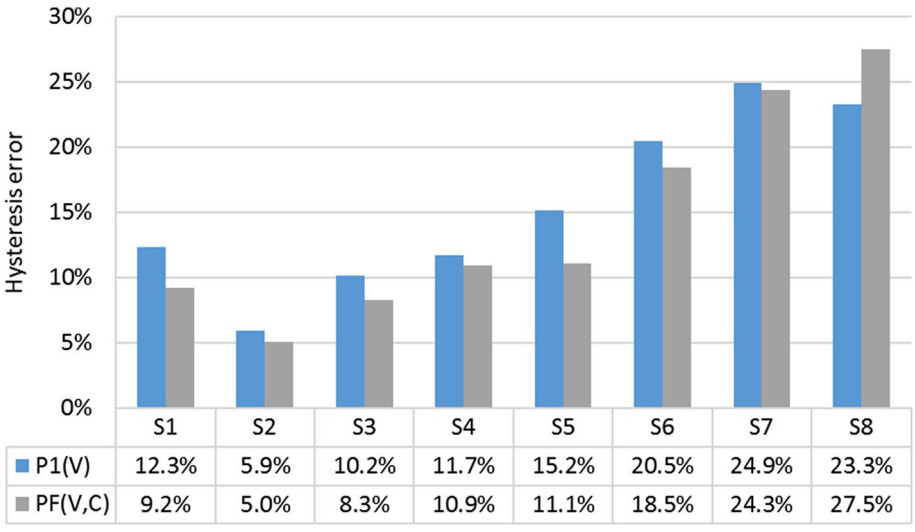

	S1	S2	S3	S4	S5	S6	S7	S8
P1(V)	12.3%	5.9%	10.2%	11.7%	15.2%	20.5%	24.9%	23.3%
PF(V,C)	9.2%	5.0%	8.3%	10.9%	11.1%	18.5%	24.3%	27.5%

Fig. 11. Comparison of normalized hysteresis errors for the sensors evaluated.

evaluated, reaching the greatest reductions, around 50%, for the sensors S1 and S5 and the lowest reduction for the sensor S6 of 5%.

6. Conclusions

In the present paper, a methodology tending to reduce the force measurement errors in force sensors Tekscan A201-1 has been implemented. The methodology was based on the measurement of the voltage and capacitance responses of the sensors when exposed to a pre-established force pattern, compared to the simple linear regression method based on the output voltage, recommended by the manufacturer.

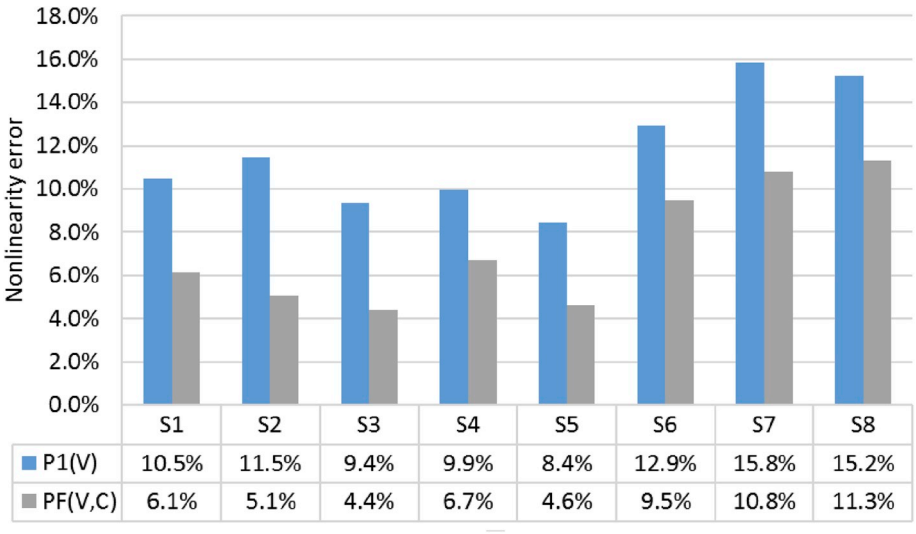

	S1	S2	S3	S4	S5	S6	S7	S8
P1(V)	10.5%	11.5%	9.4%	9.9%	8.4%	12.9%	15.8%	15.2%
PF(V,C)	6.1%	5.1%	4.4%	6.7%	4.6%	9.5%	10.8%	11.3%

Fig. 12. Comparison of normalized non-linearity errors for the sensors evaluated.

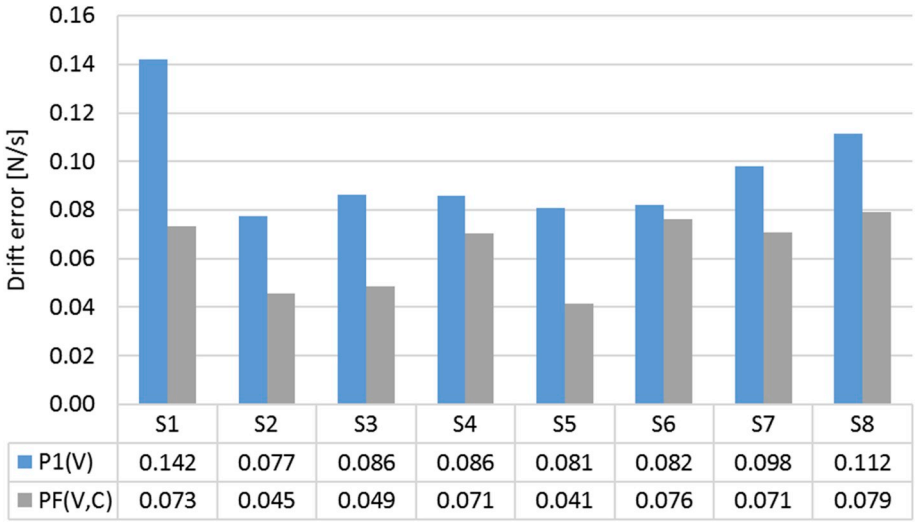

	S1	S2	S3	S4	S5	S6	S7	S8
P1(V)	0.142	0.077	0.086	0.086	0.081	0.082	0.098	0.112
PF(V,C)	0.073	0.045	0.049	0.071	0.041	0.076	0.071	0.079

Fig. 13. Comparison of normalized drift errors for the sensors evaluated.

This study was aimed at improving the response of force sensors by analyzing their hysteresis, nonlinearity and drift errors when exposed to a predefined force pattern, by implementing a correlation analysis based on a power function that considers the measurements of voltage and capacitance.

The analysis described showed that the proposed methodology allows to obtain significant reductions in the different errors considered. This contribution reduces the gap between high precision load cells and low cost FSR. It should be noted that the proposed compensation does not require additional hardware during sensor operation, which is a very desirable feature in applications with power or space limitations.

The methodology for error compensation has been developed for Tekscan A201-1 sensors. However, this procedure can be performed for sensors that exhibit a linear output, such as the Tekscan A201-X sensors, and for sensors with a non-linear response, such as the Interlink FSR40X and Peratech QTC sensors.

Acknowledgements

The authors thank the UAN University for the financing of the 2018221 project. This article is the result of the work carried out during the development of the project "Development, characterization and manufacture of luminous asphalt and the thermo-mechanical device for its application" by grant PI/UAN-2019-657REM.

Appendix A. Supplementary data

Supplementary data to this article can be found online at https://doi.org/10.1016/j.sbsr.2019.100300.

References

[1] D.M. Ştefănescu, M.A. Anghel, Electrical methods for force measurement – a brief survey, Measurement 46 (2) (Feb. 2013) 949–959.
[2] D. Fong, Y.-Y. Chan, The use of wearable inertial motion sensors in human lower limb biomechanics studies: a systematic review, Sensors 10 (12) (2010) 11556–11565, https://doi.org/10.3390/s101211556 Submitted for publication.
[3] B. Fosty, G. Ben-Sadoun, G. Sacco, A. König, V. Manera, P. Foulon, J. Brisswalter, P.H. Robert, F. Bremond, Accuracy and reliability of the RGB-D camera for measuring walking speed on a treadmill, Gait Posture 48 (Jul. 2016) 113–119, https://doi.org/10.1016/j.gaitpost.2016.04.011 Submitted for publication.
[4] C. Nüesch, E. Roos, G. Pagenstert, A. Mündermann, Measuring joint kinematics of treadmill walking and running: comparison between an inertial sensor based system and a camera-based system, J. Biomech. 57 (May 2017) 32–38, https://doi.org/10.1016/j.jbiomech.2017.03.015 Submitted for publication.
[5] G.S. Faber, A.S. Koopman, I. Kingma, C.C. Chang, J.T. Dennerlein, J.H. van Dieën, Continuous ambulatory hand force monitoring during manual materials handling using instrumented force shoes and an inertial motion capture suit, J. Biomech. 70

(Mar. 2018) 235–241, https://doi.org/10.1016/j.jbiomech.2017.10.006 Submitted for publication.
[6] J.S. Schofield, K.R. Evans, J.S. Hebert, P.D. Marasco, J.P. Carey, The effect of biomechanical variables on force sensitive resistor error: implications for calibration and improved accuracy, J. Biomech. 49 (5) (Mar. 2016) 786–792, https://doi.org/10.1016/j.jbiomech.2016.01.022 Submitted for publication.
[7] D. Guo, F. Sun, B. Fang, C. Yang, N. Xi, Robotic grasping using visual and tactile sensing, Inf. Sci. 417 (Nov. 2017) 274–286, https://doi.org/10.1016/j.ins.2017.07.017 Submitted for publication.
[8] Interlink_electronics, Data Sheet, Interlink-electronics, [Online]. Available Submitted for publication, 2018 2018 https://www.interlinkelectronics.com/request-data-sheets , Accessed date: 1 April 2019.
[9] Model A201 DatasheetTekscan Inc, FlexiForce® Force Sensor, Submitted for publication, South Boston, 2015 flexiforce-a201-datasheet. 2018.
[10] C. Lebosse, P. Renaud, B. Bayle, M. de Mathelin, Modeling and evaluation of low-cost force sensors, IEEE Trans. Robot. 27 (4) (Aug. 2011) 815–822.
[11] E.R. Komi, J.R. Roberts, S.J. Rothberg, Evaluation of thin, flexible sensors for time-resolved grip force measurement, Proc. Inst. Mech. Eng. C J. Mech. Eng. Sci. 221 (12) (Dec. 2007) 1687–1699.
[12] A.P. Anderson, D.J. Newman, Pressure sensing for in-suit measurement of space suited biomechanics, Acta Astronaut. 115 (Oct. 2015) 218–225.
[13] M.F. Antwi-Afari, H. Li, Fall risk assessment of construction workers based on biomechanical gait stability parameters using wearable insole pressure system, Adv. Eng. Inf. 38 (Oct. 2018) 683–694.
[14] J.F. Drazan, O.T. Abdoun, M.T. Wassick, R. Dahle, L. Beardslee, G.A. Marcus, N.C. Cady, E.H. Ledet, Simple implantable wireless sensor platform to measure pressure and force, Med. Eng. Phys. 59 (Sep. 2018) 81–87.
[15] J. Rueterbories, E.G. Spaich, B. Larsen, O.K. Andersen, Methods for gait event detection and analysis in ambulatory systems, Med. Eng. Phys. 32 (6) (Jul. 2010) 545–552.
[16] T. Schmeltzpfenning, T. Brauner, Foot biomechanics and gait," Handb. Footwear Des. Manuf. (Jan. 2013), pp. 27–48.
[17] A. Beyaz, Harvest glove and LabView based mechanical damage determination on apples, Sci. Hortic. (Amst.) 228 (Jan. 2018) 49–55.
[18] R.K.-Y. Tong, M.N. Victorino, X. Jiang, C. Menon, "Wearable Technologies and Force Myography for Healthcare," in *Wearable Technology In Medicine And Health Care*, Academic Press, 2018, pp. 135–152.
[19] J.G. Dabling, A. Filatov, J.W. Wheeler, "Static and cyclic performance evaluation of sensors for human interface pressure measurement," in *2012*, Annual International Conference of the IEEE Engineering in Medicine and Biology Society, vol. 2012, 2012, pp. 162–165.
[20] L. Paredes-Madrid, A. Matute, A.F. Cruz-Pacheco, C.A. Parra-Vargas, Elkin, I. Gutiérrez-Velásquez, Experimental characterization, modeling and compensation of hysteresis in force sensing resistors, Rev. DYNA 85 (205) (2018) 191–198.
[21] A.G. Herbert-Copley, E.H. Sinitski, E.D. Lemaire, N. Baddour, Temperature and measurement changes over time for F-Scan sensors, In 2013 IEEE International Symposium on Medical Measurements and Applications, MeMeA), 2013, pp. 265–267.
[22] A.A. Polliack, R.C. Sieh, D.D. Craig, S. Landsberger, D.R. McNeil, E. Ayyappa, Scientific validation of two commercial pressure sensor systems for prosthetic socket fit, Prosthet. Orthot. Int. 24 (1) (Apr. 2000) 63–73.
[23] C. Visone, Hysteresis modelling and compensation for smart sensors and actuators, J. Phys. Conf. Ser. 138 (1) (Nov. 2008) 012028.
[24] S. Urban, M. Ludersdorfer, P. van der Smagt, Sensor calibration and hysteresis compensation with heteroscedastic Gaussian processes, IEEE Sens. J. 15 (11) (Nov. 2015) 6498–6506.
[25] L. Paredes-Madrid, L. Emmi, E. Garcia, P.G. de Santos, Detailed study of amplitude nonlinearity in piezoresistive force sensors, Sensors 11 (9) (2011) 8836–8854.
[26] A. Melnyk, P. Henaff, V. Khomenko, V. Borysenko, Sensor network architecture to measure characteristics of a handshake between humans, IEEE 34th International Scientific Conference on Electronics and Nanotechnology, ELNANO), 2014, pp. 264–268 2014.
[27] Esteco.com, "modeFrontier 4.0,", [Online]. Available: https://www.esteco.com/modefrontier, (2008) , Accessed date: 1 April 2019.
[28] R. Rizvi, B. Cochrane, E. Biddiss, H.- Naguib, Piezoresistance characterization of poly(dimethyl-siloxane) and poly(ethylene) carbon nanotube composites, Smart Mater. Struct. 20 (9) (2011).
[29] Y. Hou, D. Wang, X. Zhang, H. Zhao, J. Zha, Z. Dang, Positive piezoresistive behavior of electrically conductive alkyl-functionalized graphene/poly-dimethylsilicone nanocomposites, J. Mater. Chem. 1 (3) (2013), https://doi.org/10.1039/C2TC00114D.
[30] J. Hidalgo-Lopez, O. Oballe-Peinado, J. Castellanos-Ramos, J. Sanchez-Duran, R. Fernandez-Ramos, F. Vidal-Verdu, High-Accuracy Readout Electronics for Piezoresistive Tactile Sensors, Sensors 17 (11) (2017), https://doi.org/10.3390/s17112513.
[31] US Patent US5989700A, Pressure sensitive ink means, and methods of use, (1996).
[32] US6272936B1, Pressure sensor, (1999).
[33] M. Saadeh, M. Trabia, Identification of a force-sensing resistor for tactile applications, J. Intell. Mater. Syst. Struct. 24 (7) (2013), https://doi.org/10.1177/1045389X12463462.